Numerical study of the collapse of columns of sand immersed in water using two-phase flow modeling

Anouk Riffard, Miltiadis V. Papalexandris

Institute of Mechanics, Materials and Civil Engineering
Université catholique de Louvain
1348 Louvain-la-Neuve, Belgium

Abstract

In this paper we present a numerical study of the collapse of a column of sand immersed in water. It consists of two-dimensional simulations and is based on a recently developed two-phase thermomechanical theory for granular suspensions. For the shear viscosity of the granular phase, we have tested various parameterizations and selected the one that gave better comparisons with experiments. Our study focuses on the influence of the initial volume fraction and the aspect ratio of the column. The shape of the final deposit, the final-to-initial height ratio, as well as the runout distance and amount of suspended sand are found to be dependent on both parameters. In densely-packed columns, the collapse always starts with the detachment and falling of the top corner. The final deposit is trapezoidal for small and intermediate aspect ratios and triangular for high ones. On the contrary, in loosely-packed columns, the entire lateral side falls while the rest of the column descends and compacts due to its own weight. For loose packings, the final deposit is always trapezoidal for the aspect ratios considered herein, while the final-to-initial height ratio is also considerably lower than for dense packings. Also, the amount of suspended sand is significantly higher for loose packings and it also increases with the aspect ratio. Our numerical predictions are in good agreement with earlier published data on the collapse of sand columns immersed in water.

Keywords: granular materials, granular-column collapse, sand, granular suspensions, granular rheology

1. Introduction

Granular materials are ubiquitous in nature and many phenomena involve the release of large quantities of them: sediment transport, sand motion, landslides, debris flows etc. Several of those events constitute major hazards for populations, economy and ecosystems [1]. Granular materials are also used in many industrial applications such as chemical, food and pharmaceutical processes. Their diversity and versatility make them the second most used class of materials in the industry, right behind water [2]. However, they often exhibit counter-intuitive behaviour and many of their features are still not well understood.

In the past, various experimental studies were conducted to provide insight into the flow of granular materials. A number of them focused on laboratory-scale experiments of an archetypal type of such flows; namely, the collapse of granular columns. In fact, this phenomenon has been frequently used as a benchmark test using both axisymmetric [3, 4] and 2D configurations [5, 6]. The first studies of granular-column collapse that appeared in the literature focused on cases in which the surrounding fluid was a gas (typically air) and, therefore, its density was much lower than that of the solid material. Such mixtures are referred to as *dry granular materials* and quite often the effect of the surrounding gas does not significantly impact the motion of the grains. Contact interactions between grains are then the dominant forces while hydrodynamic interactions can be neglected. In dry granular columns, the aspect ratio has been identified as the main parameter influencing their collapse, whereas other parameters such as the grains diameter and the initial volume fraction have been found to play only a minor role [7, 8]. In fact, a wealth of studies have reported that the horizontal spreading and deposition of the granular material, also known as *runout distance*, the final height and the duration of the collapse could be given in terms of a power-law of the initial aspect ratio only; see, for example [3, 4, 5, 6, 9, 10].

While the collapse of dry granular columns has been studied extensively, the case where the surrounding fluid is a liquid has been proven to be more challenging. Thompson and Huppert [11] were among the first authors to report on experiments with sand columns immersed in water and to compare with the dry column collapse. As mentioned in [1], during the collapse of immersed columns occurring in nature, contact interactions are still significant because the initial volume fraction $\phi_{\mathrm{s,i}}$ is quite high, typically in the range between 0.5 and 0.6. However, the presence of a fluid whose density is of the

same order of magnitude as that of the particles leads to complex hydrodynamic interactions between the two phases. As a consequence, the interstitial fluid plays a crucial role in the column collapse [12], especially when momentum advection and interphasial drag are significant [13]. The effect of the interstitial fluid is thus dual; on the one hand it tends to lubricate the grains, thereby reducing friction and enhancing the flow. On the other hand, as it was shown in [14], it slows down the collapse through interphasial drag. The authors of [13] derived a two-phase model to characterize and quantify these effects, and concluded that the dynamics of the granular phase cannot be captured without considering the fluid pressure and the interactions through interphasial forces. Accurate modeling of this type of flows still remains an open problem nowadays.

Despite those complexities, several experimental studies concerned with the collapse of granular columns in liquids are available in the literature. A well-known one is the large-scale experiment of Iverson [15] which highlighted the different behavior of loosely and densely-packed columns, $\phi_{\mathrm{s,i}} \approx 0.55$ and $\phi_{\mathrm{s,i}} \approx 0.59$ respectively. While in the latter case the column slowly crumbles in different blocks, in the former one it suddenly flows like a liquid. Subsequently, the properties of granular collapse under loose and dense packings have been examined in a number of experimental studies; see, for example, [16, 17, 18, 19, 20, 21]. In recent years, granular collapse has also been studied numerically via different modeling approaches. In particular, the studies [22, 23, 24] involved discrete-element simulations, whereas [16, 25] were based on mixture models and [12, 26, 27, 28, 29] on two-phase flow models.

However, most of the studies available in the literature considered glass beads and not sand [18, 19, 26, 22, 16, 24]. The rheological behaviour of glass beads is documented in more detail because beads can be reasonably approximated by hard spheres. On the other hand, natural sand is more heterogeneous and its rheological properties are expected to be different than those of hard spheres. It is also worth mentioning that some authors considered a mixture of water and Ucon oil 75H90000, which is much more viscous than water [17, 18, 19, 30]. A more viscous fluid is expected to dampen interactions between the two phases by considerably slowing down the collapsing process [19, 31].

The aforementioned studies highlighted the key role of the initial volume fraction, *i.e.* the initial packing, on the collapse of a granular column immersed in a liquid. For example, Rondon et al. [18] have pointed out that, unlike dry cases, the shape of the final deposit, the duration of the collapse

and the runout distance are significantly influenced by the initial volume fraction. Further, whereas in the collapse of dry columns the initial aspect ratio is found to be the most important parameter for the collapse, the available results for columns immersed in a liquid are less conclusive. In some studies [22, 30] it was reported that the aspect ratio plays an important role in the dynamics of the collapse, while in some others [18] it was mentioned that its role is not significant compared to that of the initial packing. It is worth noting, however, that those studies involved different mixtures and therefore, the influence of the aspect ratio might as well be material-dependent.

In this paper we present detailed numerical simulations of the collapse of laboratory-scale sand columns, immersed in water, under their own weight. The main objective is to provide new physical insight of the problem in hand and to examine the role of the initial volume fraction and the aspect ratio. Comparisons of our numerical results with the scarce experimental data for water-sand mixtures are also provided herein and show good agreement.

The simulations are based on a two-velocity, two-pressure thermomechanical model for granular suspensions [32]. This model is deemed capable of capturing important features of granular suspensions such as dilatancy, compaction and non-Newtonian rheology [33]. Our choice of adopting a two-phase approach is motivated by the fact that single-phase mixture models have been acknowledged for not being able to accurately capture the interactions between the two phases when the surrounding fluid plays a non-negligible role [34]. Nonetheless, numerical simulations with two-velocity, two-pressure models and nonlinear granular rheology are particularly scarce.

It is also worth mentioning that particular attention has been paid to the parametrization of the shear viscosity of the granular phase. Since relevant data are not readily available in the literature, we have extracted a number of correlations from existing models for the shear viscosity of the mixture, *i.e.* for the suspension viscosity [35]. In the context of our study, we have compared the numerical predictions with those correlations for the mixture in hand and selected the one that gave better comparisons with experiments. The results of these comparisons are also presented herein.

The paper is organised as follows. In Section 2, we present the governing equations and outline the algorithm for their numerical treatment. In Section 3, we provide correlations for the various viscosity coefficients of the granular phase and discuss in detail the parametrization of the shear viscosity. Subsequently, in Section 4, we present and discuss our numerical results; this section contains a description of the various stages of the collapse, compar-

isons with experiments and the parametric studies with respect to the initial volume fraction and the aspect ratio. Finally, Section 6 concludes.

2. Governing equations

The model used herein is based on the two-phase thermomechanical theory for granular suspensions presented in [32] which yields a two-velocity, two-pressure system of governing equations. The reason for adopting this approach is that the velocities of the two phases can be substantially different, especially during transient phenomena such as gravity-induced motion of particles or remobilization of sediments. The velocity difference can be explained by the fact that since the two phases have in general different densities, then their gravitational accelerations will also be different. Therefore, a two-velocity formulation is better adapted to properly capture the transient phenomena of interest, which constitutes a significant advantage compared to one-velocity counterparts.

In order to fix ideas, let us consider a mixture of an isotropic granular solid and a Newtonian fluid, where both phases have constant densities. The subscripts 'f' and 's' in the symbols appearing herein refer to the fluid and solid granular phases, respectively. Therefore, the volume fractions of the granular and fluid phases will be denoted as ϕ_s and ϕ_f. Moreover, the mixture is assumed to be saturated, in other words,

$$\phi_\mathrm{s} + \phi_\mathrm{f} \;=\; 1\,. \tag{1}$$

Each phase is described as a continuum with its own set of governing equations. The mass and momentum balance laws for each phase thus read as follows.

Fluid phase

$$\frac{\partial \phi_\mathrm{f}}{\partial t} + \nabla\cdot(\phi_\mathrm{f}\boldsymbol{u}_\mathrm{f}) \;=\; 0\,, \tag{2}$$

$$\rho_\mathrm{f}\frac{\partial \phi_\mathrm{f}\boldsymbol{u}_\mathrm{f}}{\partial t} + \rho_\mathrm{f}\nabla\cdot(\phi_\mathrm{f}\boldsymbol{u}_\mathrm{f}\otimes\boldsymbol{u}_\mathrm{f}) \;=\; \nabla\cdot\boldsymbol{\sigma}_\mathrm{f} - \boldsymbol{f} + \rho_\mathrm{f}\phi_\mathrm{f}\boldsymbol{g}\,. \tag{3}$$

Solid phase

$$\frac{\partial \phi_\mathrm{s}}{\partial t} + \nabla\cdot(\phi_\mathrm{s}\boldsymbol{u}_\mathrm{s}) \;=\; 0\,, \tag{4}$$

$$\rho_\mathrm{s}\frac{\partial \phi_\mathrm{s}\boldsymbol{u}_\mathrm{s}}{\partial t} + \rho_\mathrm{s}\nabla\cdot(\phi_\mathrm{s}\boldsymbol{u}_\mathrm{s}\otimes\boldsymbol{u}_\mathrm{s}) \;=\; \nabla\cdot\boldsymbol{\sigma}_\mathrm{s} + \boldsymbol{f} + \rho_\mathrm{s}\phi_\mathrm{s}\boldsymbol{g}\,. \tag{5}$$

In the above equations, ρ_i, $\boldsymbol{u}_i$ and $\boldsymbol{\sigma}_i$ stand for the density, velocity vector and stress tensor of the phase i, respectively. Additionally, $\boldsymbol{g}$ is the gravitational acceleration. As mentioned above, the surrounding fluid is considered to be a simple Newtonian one. As such, its stress tensor is the sum of only two contributions, namely,

$$\boldsymbol{\sigma}_\mathrm{f} \;=\; -p_\mathrm{f}\phi_\mathrm{f}\boldsymbol{I} + \boldsymbol{\tau}_\mathrm{f}\,, \tag{6}$$

where p_f is the fluid pressure, $\boldsymbol{I}$ is the identity tensor and $\boldsymbol{\tau}_\mathrm{f}$ is the viscous-stress tensor. For simple isotropic fluids, $\boldsymbol{\tau}_\mathrm{f}$ is further decomposed as the sum of a diagonal and a deviatoric component,

$$\boldsymbol{\tau}_\mathrm{f} \;=\; \phi_\mathrm{f}\,\zeta_\mathrm{f}\,(\nabla\cdot\boldsymbol{u}_\mathrm{f})\boldsymbol{I} + 2\phi_\mathrm{f}\,\mu_\mathrm{f}\,\boldsymbol{D}_\mathrm{f}^\mathrm{d}\,, \tag{7}$$

where $\boldsymbol{D}_\mathrm{f}^\mathrm{d}$ is the deviatoric component of the strain rate tensor $\boldsymbol{D}_\mathrm{f}$, which reads $\boldsymbol{D}_\mathrm{f} = \frac{1}{2}\left(\nabla\boldsymbol{u}_\mathrm{f} + (\nabla\boldsymbol{u}_\mathrm{f})^\top\right)$. In this relation, ζ_f and μ_f are, respectively, the bulk and shear viscosities of the fluid. It is interesting to note that the bulk viscous pressure is not zero, unlike in the cases of constant-density, single-phase flows. Indeed, the velocity field for the fluid phase is non-solenoidal, *i.e.* $\nabla\cdot\boldsymbol{u}_\mathrm{f} \neq 0$, while the bulk viscosity of the fluid of interest (water) is not negligible.

The stress tensor of the solid phase is modeled as the sum of three contributions: the pressure p_s, an additional elastic stress tensor $\boldsymbol{C}_\mathrm{s}$ related to the microstructure of the solid phase (sometimes referred to as *configuration stress tensor*), and a dissipative (viscous) stress tensor $\boldsymbol{\tau}_\mathrm{s}$,

$$\boldsymbol{\sigma}_\mathrm{s} \;=\; -\phi_\mathrm{s}p_\mathrm{s}\boldsymbol{I} + \boldsymbol{C}_\mathrm{s} + \boldsymbol{\tau}_\mathrm{s}\,. \tag{8}$$

According to [32] the constitutive expression for the tensor $\boldsymbol{C}_\mathrm{s}$ reads

$$\boldsymbol{C}_\mathrm{s} \;=\; \gamma_\mathrm{s}\nabla\phi_\mathrm{s}\otimes\nabla\phi_\mathrm{s}\,, \tag{9}$$

where the coefficient γ_s accounts for the spatial distribution of the grains and, therefore, depends on ϕ_s; see also [36, 37].

The granular phase is known to exhibit non-Newtonian rheological behaviour, *i.e.* the granular viscous stresses are nonlinear functions of the strain rate tensor. Monsorno et al. [32] proposed the following constitutive law for these stresses,

$$\boldsymbol{\tau}_\mathrm{s} \;=\; \left(\left(\zeta_\mathrm{s}+\zeta_{\mathrm{s}'}\right)\nabla\cdot\boldsymbol{u}_\mathrm{s} + \chi_1\right)\phi_\mathrm{s}\boldsymbol{I} + 2\left(\mu_\mathrm{s}+\mu_{\mathrm{s}'}\right)\phi_\mathrm{s}\boldsymbol{D}_\mathrm{s}^\mathrm{d} + \chi_2\phi_\mathrm{s}\boldsymbol{D}_\mathrm{s}\cdot\boldsymbol{D}_\mathrm{s}\,. \tag{10}$$

In this relation, $\mu_{\rm s}$ and $\zeta_{\rm s}$ are, respectively, the shear viscosity and bulk viscosity coefficients, by analogy with $\mu_{\rm f}$ and $\zeta_{\rm f}$. The terms involving the parameters $\zeta_{\rm s'}$, $\mu_{\rm s'}$, χ_1 and χ_2 describe the non-Newtonian rheology of the granular phase. In particular, all these parameters are nonlinear functions of the strain-rate tensor and read as follows,

$$\mu_{\rm s'} \;=\; \frac{\mu_{\rm n}}{\sqrt{2}}\frac{\det \boldsymbol{D}_{\rm s}}{(\boldsymbol{D}_{\rm s}:\boldsymbol{D}_{\rm s})^{\frac{3}{2}}}\,, \qquad \zeta_{\rm s'} \;=\; \frac{\mu_{\rm n}\sqrt{2}}{3}\frac{\det \boldsymbol{D}_{\rm s}}{(\boldsymbol{D}_{\rm s}:\boldsymbol{D}_{\rm s})^{\frac{3}{2}}}\,, \tag{11}$$

$$\chi_1 \;=\; -\sqrt{2}\mu_{\rm n}\left(2\sqrt{\boldsymbol{D}_{\rm s}^{\rm d}:\boldsymbol{D}_{\rm s}^{\rm d}} - \frac{3}{2}\frac{\boldsymbol{D}_{\rm s}^{\rm d}:\boldsymbol{D}_{\rm s}^{\rm d}}{\sqrt{\boldsymbol{D}_{\rm s}:\boldsymbol{D}_{\rm s}}}\right)\,, \quad \chi_2 \;=\; -\frac{\sqrt{2}\mu_{\rm n}}{\sqrt{\boldsymbol{D}_{\rm s}:\boldsymbol{D}_{\rm s}}}\,, \tag{12}$$

where the symbol : stands for the double inner product between two second-order tensors. In absence of assertive experimental data, the coefficient $\zeta_{\rm s}$ is taken to be proportional to $\mu_{\rm s}$. The parameterizations of $\mu_{\rm s}$ and $\mu_{\rm n}$ that are employed herein are elaborated in detail in section 3 below.

Further, in equations (3) and (5), $\boldsymbol{f}$ represents the interaction force between the two phases. It is composed of a non-dissipative and a dissipative component,

$$\boldsymbol{f} \;=\; p_{\rm f}\nabla\phi_{\rm s} + \delta(\boldsymbol{u}_{\rm f}-\boldsymbol{u}_{\rm s})\,, \tag{13}$$

The buoyancy (or nozzling) term, $p_{\rm f}\nabla\phi_{\rm s}$, is the non-dissipative component. The second term, $\delta(\boldsymbol{u}_{\rm f}-\boldsymbol{u}_{\rm s})$, is the dissipative component, with δ being the "drag" coefficient. In [38] the authors examined the effects of inertia to the interaction force and their scaling with the particle Reynolds number. Thus, inertial effects can be taken into account via an appropriate expression for δ. To this end, we employ the correlation for δ proposed in [39], which is valid for a wide range of volume fractions and particle Reynolds numbers, so as to account for inertia effects.

Additional dissipative terms can be added to $\boldsymbol{f}$ and their constitutive expressions have been reviewed in [40]. For example, terms involving velocity gradients can be added to represent Faxen forces [41]. Herein, those extra terms are omitted for purposes of simplicity and also because we assume that they are small compared to the corresponding shear components of $\boldsymbol{\sigma}_{\rm s}$ and $\boldsymbol{\sigma}_{\rm f}$. Finally, we note that the expressions of $\boldsymbol{\sigma}_{\rm s}$ and $\boldsymbol{\sigma}_{\rm f}$ involve the corresponding volume fraction and, therefore, the coupling between volume-fraction and velocity gradients is in fact included in our model.

The above system of balance laws (2)-(5) is closed with an evolution equation for the volume fraction $\phi_{\rm s}$. This equation is sometimes referred to

as *compaction equation* and, according to the model [32], reads,

$$\frac{\partial \phi_{\mathrm{s}}}{\partial t} + \boldsymbol{u}_{\mathrm{s}} \cdot \nabla \phi_{\mathrm{s}} \;=\; Re \frac{\phi_{\mathrm{s}}\, \phi_{\mathrm{f}}}{\mu_{\mathrm{c}}} \left(p_{\mathrm{s}} - p_{\mathrm{f}} - \beta_{\mathrm{s}} + \nabla \cdot (\gamma_{\mathrm{s}} \nabla \phi_{\mathrm{s}}) \right) . \tag{14}$$

This form of the compaction equation is deemed capable of capturing important features of granular materials such as dilatancy and contraction. The microstructure of the granular phase is accounted for via γ_{s}, which was mentioned above, and β_{s}. In particular, β_{s} is referred to as *intergranular stress* and describes the resistance of grains to compaction. Moreover, the quantity μ_{c} accounts for the dissipative relaxation due to the compaction occurring in the solid phase. It is often referred to as *compaction viscosity* since it has dimensions of viscosity.

With regard to the constitutive expression for γ_{s}, we employ a simple power law which reads,

$$\gamma_{\mathrm{s}} \;=\; -\gamma_0\, \phi_{\mathrm{s}}^6 \,, \tag{15}$$

where γ_0 is a positive material-dependent constant. The sixth-power law was chosen because its predictions were in good agreement with experimental data for pressure-driven granular suspensions [42]. This constitutive expression was also used in [33].

The correlation used for β_{s} is also of empirical nature. Since β_{s} represents the resistance of grains to compaction, it is expected to diverge when ϕ_{s} tends to its maximum value ϕ_{m} (*i.e.* at maximum packing) and to vanish when ϕ_{s} approaches zero. The expression used in this study is a simplified version of that derived in [43] and is given by,

$$\beta_{\mathrm{s}} \;=\; -\beta_0 \ln \left(\frac{\phi_{\mathrm{m}} - \phi_{\mathrm{s}}}{\phi_{\mathrm{m}}} \right) , \tag{16}$$

where β_0 is a positive material-dependent constant. It is worth noting that this relation becomes singular at the jamming limit, *i.e.* at the maximum packing of grains $\phi_{\mathrm{s}} = \phi_{\mathrm{m}}$.

For a detailed derivation of the thermomechanical two-phase flow model used in this study, the reader is referred to [32].

The numerical algorithm used to solve the aforementioned equations is based on a predictor-corrector time integration scheme, coupled with a generalised projection method for the pressure of each phase [28]. The projection method was first introduced by Chorin [44] and Temam [45] independently

for the numerical treatment of the (constant-density) Navier-Stokes equations. The so-called projection step amounts to combining the divergence of the momentum equation with the continuity equation, allowing a decoupling of the computation of the pressure from that of the velocity. When applied to the Navier-Stokes equations, this procedure yields a Poisson equation for the pressure and relies on the fact that the velocity field is divergence free. In the equations considered herein, the velocity fields of both phases are non-solenoidal, which means that the projection method leads to a second-order elliptic equation for each phasial pressure.

Further, the algorithm employs a finite-volume discretization of the governing equations in a collocated grid. The advantages of collocated grids over staggered ones are computational simplicity and straightforward extension of the method to curvilinear coordinate systems. However, they can produce spurious oscillations of the pressure field; this is the well known *odd-even decoupling* problem. To address it, we employ a flux-interpolation technique for the convective fluxes, which are computed at the cell interfaces by combining the values of the velocities, volume fractions and pressure gradients. This procedure is a generalized formulation of the original Rhie-Chow interpolation scheme [46] and is described in [47, 48].

The algorithm has been implemented in a 3D parallel code written in C/C++ and employs PETSc suites of data structures and routines for the scalable parallel solution of partial differential equations via the Message Passing Interface (MPI) protocol [49, 50]. More specifically, the linear systems arising from the discretization of the equations (2)-(5) and (14) are solved using the Generalized MinResidual (GMRES) scheme with variations of the algebraic multigrid method as preconditioners. For an extensive description of the numerical method for the governing system consisting of equations (2)-(5) and (14), the reader is referred to [28].

3. Correlations for the viscosity coefficients of the granular phase

This section is concerned with the parametrization of the viscosity coefficients of the granular phase that appear in equation (10). First we elaborate on the derivation of a correlation for the shear viscosity μ_{s}. Then we present the correlations for the bulk and normal viscosities, ζ_{s} and μ_{n} respectively, as well as for the so-called compaction viscosity μ_{c}.

3.1. Shear viscosity

Numerical tests that we performed in the framework of our study have indicated that the parametrization of μ_s plays an important role for the reliable simulation of the flows of interest. However, there are no readily available correlations for this parameter but only for the suspension viscosity, *i.e.* for the shear viscosity of the mixture, μ_{sus}. Therefore, we have to derive an expression for μ_s for sand from available correlations for the suspension viscosity. This procedure requires an assumption about the relative "weight" of μ_s to that of the suspension.

To this end we follow Morris & Boulay [51] who decomposed the suspension viscosity coefficient into the sum of the fluid shear viscosity coefficient and an additional term which they referred to as the "*particle contribution to the shear viscosity*". In our case, we identify this contribution mentioned in [51] as $\phi_s \mu_s$. Evidently, this is an *ad hoc* approach and, therefore, its applicability has certain limitations. Nonetheless, in view of the lack of relevant experimental data, it is deemed a sensible approach for deriving the sought-after correlation for μ_s.

This choice is also motivated from the fact that for any given material surface, the stress tensor of the granular phase acts only on the part of the surface occupied by this particular phase. Therefore, the granular stress tensor should be proportional to ϕ_s, as per equation (10). Accordingly, we assume the following relation between the suspension viscosity and those of the two phases,

$$\mu_{sus} \;=\; \mu_f + \mu_s \, \phi_s \, . \tag{17}$$

Then, correlations for μ_s can be derived from those for μ_{sus} via the above equation.

Since Einstein's analysis of dilute suspensions [52], numerous efforts have been made to provide accurate correlations for the suspension viscosity. For example, the Batchelor [53] and Roscoe-Brinkman [54, 55] models are extensions of the Einstein relation that include higher-order powers of ϕ_s. Still, these models are valid only in the dilute regime, *i.e.* $\phi_s \ll 1$. Subsequently, various models were put forward that are applicable to a wide range of volume fractions, including dense mixtures. Crucially, the more recent models satisfy the constraint of diverging (singular) behaviour when ϕ_s approaches the jamming limit ϕ_m.

In Table 1, we provide some well-known correlations available for the viscosity of suspensions. In this table, η_r is the relative viscosity, defined as

the ratio between the suspension and fluid viscosities, *i.e.* $\eta_{\mathrm{r}} = \frac{\mu_{\mathrm{sus}}}{\mu_{\mathrm{f}}}$. The original correlations of Krieger-Dougherty [56] and Quemada [57] correspond, respectively, to the first terms of the so-called *modified Krieger-Dougherty* and *modified Quemada* models shown in Table 1. Those original correlations diverge when $\phi_{\mathrm{s}} \to \phi_{\mathrm{m}}$, but do not follow the expected asymptotic behaviour of μ_{sus} at small ϕ_{s} on the basis of available experimental data. Dörr et al. [58] remedied this issue and captured the right asymptotic behaviour in the dilute regime by adding additional power terms in the original correlations. It is worth adding that all the models listed in Table 1 (except that of Einstein) also tend to 0 when $\phi_{\mathrm{s}} \to 0$ and to infinity when $\phi_{\mathrm{s}} \to \phi_{\mathrm{m}}$.

We further note that the model of Boyer et al. [59] is the ϕ_{s}-dependent formulation of the popular $\mu(I)$-rheology law, which was originally cast as a function of the so-called *viscous number* I_v. Actually, this model was initially developed for dry granular materials [62, 63] and was proved appropriate for dry granular collapse [64, 9]. Since then, it has been extended to granular suspensions [16, 59]; see also [24].

In Figure 1, we present plots of the shear viscosity of the solid phase μ_{s} as a function of the volume fraction, on the basis of the correlations for the suspension viscosity provided in Table 1 and equation (17). The maximum volume fraction has been set to $\phi_{\mathrm{m}} = 0.60$. This value was found to be the most appropriate one for the mixture of interest (sand and water) and is in agreement with the values provided in [65] for random close packings.

From these plots, we observe that all the curves collapse into a single one that tends to zero as $\phi_{\mathrm{s}} \to 0$. With regard to the other jamming limit, $\phi_{\mathrm{s}} \to \phi_{\mathrm{m}}$, all the curves diverge to infinity in the vicinity of the maximum volume fraction, $\phi_{\mathrm{m}} = 0.60$, except of course for the Einstein relation which is valid in the dilute regime only. We also note that the Morris-Boulay model gives higher values at low and moderate volume fractions, but then coincides with the modified Krieger-Dougherty curve. The μ_{s} curve according to the model of Boyer et al. [59] is very close to that of Eilers [60]. Also, the Eilers, Boyer et al. and modified Quemada models diverge the most rapidly as $\phi_{\mathrm{s}} \to \phi_{\mathrm{m}}$. Overall, the predictions of the various correlations considered herein differ considerably over the entire range of volume fractions, except in the dilute limit.

We further note that μ_{s} is a material dependent property; for example, the shear viscosity of sand is different than that of hard glass spheres. In order to choose the most suitable correlation for μ_{s} for water-sand mixtures,

Correlation	Equation
Einstein [52]	$\eta_{\mathrm{r}} = 1 + \eta_1 \, \phi_{\mathrm{s}}$
Modified Krieger-Dougherty [58]	$\eta_{\mathrm{r}} = \left(1 - \frac{\phi_{\mathrm{s}}}{\phi_{\mathrm{m}}}\right)^{-\eta_1 \phi_{\mathrm{m}}} + \left(\eta_2 - \eta_1 \frac{1 + \eta_1 \phi_{\mathrm{m}}}{2\phi_{\mathrm{m}}}\right) \phi_{\mathrm{s}}^2$
Modified Quemada [58]	$\eta_{\mathrm{r}} = \left(1 - \frac{\phi_{\mathrm{s}}}{\phi_{\mathrm{m}}}\right)^{-2} + \left(\eta_1 - \frac{2}{\phi_{\mathrm{m}}}\right) \phi_{\mathrm{s}} + \left(\eta_2 - \frac{3}{\phi_{\mathrm{m}}^2}\right) \phi_{\mathrm{s}}^2$
Boyer et al. [59]	$\eta_r = 1 + \eta_1 \phi_{\mathrm{s}} \left(1 - \frac{\phi_{\mathrm{s}}}{\phi_{\mathrm{m}}}\right)^{-1} + \mu^c(\phi_{\mathrm{s}}) \left(\frac{\phi_{\mathrm{s}}}{\phi_{\mathrm{m}} - \phi_{\mathrm{s}}}\right)^2$
	$\mu^c = \mu_1 + \frac{(\mu_2 - \mu_1)}{[1 - I_0 \phi_{\mathrm{s}}^2 (\phi_{\mathrm{m}} - \phi_{\mathrm{s}})^{-2}]}$
Eilers [60]	$\eta_{\mathrm{r}} = \left(1 + \frac{1}{2} \eta_1 \left(\frac{\phi_{\mathrm{s}}}{1 - \phi_{\mathrm{s}}/\phi_{\mathrm{m}}}\right)\right)^2$
Morris & Boulay [51]	$\eta_{\mathrm{r}} = 1 + \frac{\eta_1 \phi_{\mathrm{s}}}{1 - \phi_{\mathrm{s}}/\phi_{\mathrm{m}}} + K_{\mathrm{s}} \frac{(\phi_{\mathrm{s}}/\phi_{\mathrm{m}})^2}{(1 - \phi_{\mathrm{s}}/\phi_{\mathrm{m}})^2}$

Table 1: Correlations for the relative viscosity $\eta_{\mathrm{r}} = \frac{\mu_{\mathrm{sus}}}{\mu_{\mathrm{f}}}$ of the suspension as a function of the volume fraction of the solid phase ϕ_{s}. For the case considered here, $\eta_1 = 2.5$, $\eta_2 = 5.2$ [61], $\mu_1 = 0.32$, $\mu_2 = 0.7$, $I_0 = 0.005$ [59], $K_{\mathrm{s}} = 0.1$ and $\phi_{\mathrm{m}} = 0.60$.

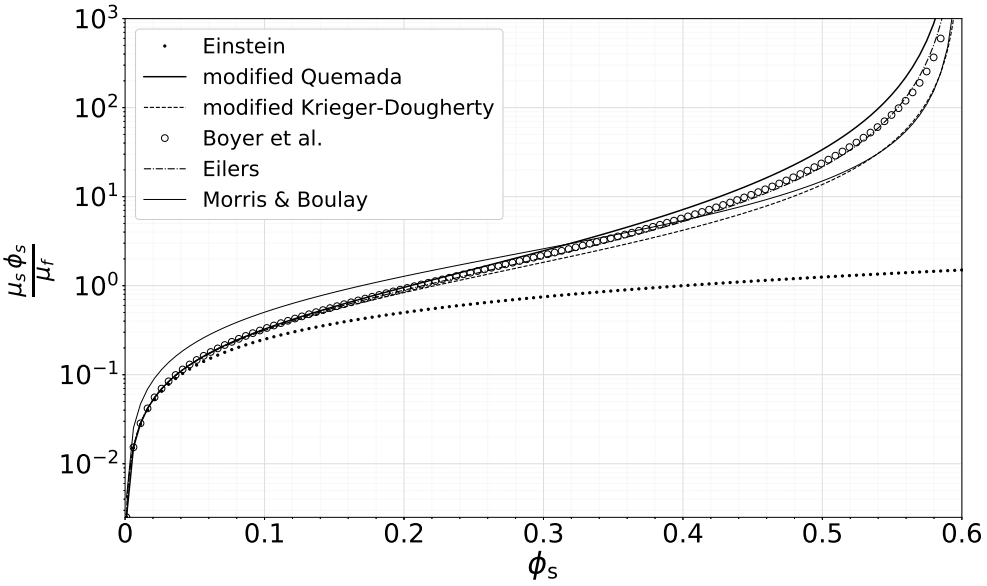


Figure 1: Evolution of the dimensionless shear viscosity of the solid phase, scaled by μ_f, as a function of the volume fraction for different viscosity laws: Einstein [52], modified Quemada [58], modified Krieger-Dougherty [56], Boyer et al. [59], Eilers [60] and Morris & Boulay [51].

we performed simulations of granular column collapse using the correlations listed in Table 1. We observed significant differences between the numerical results, which corroborates the fact that μ_s plays a major role in the behaviour of granular piles. More specifically, for loosely-packed columns with $\phi_\mathrm{s} = 0.554$, there was no remnant pile with the modified Krieger-Dougherty model and the height of the remnant pile was too low with the Morris & Boulay model.

For densely-packed columns, the heights of the remnant pile predicted with the modified Quemada [58], Eilers [60] and Boyer et al. [59] models were considerably higher than with the other models and satisfactorily close to experimental data. This is not surprising considering that these three models predict the highest values of μ_s for dense suspensions, as shown in Figure 1. The final deposits obtained using these three models are shown on Figure 2. All three of them predicted a remnant pile that resembles the one in the experiments [11].

Also, when compared against the experimental data [11] for the angle of repose and the final height of the remnant pile, the numerical predictions

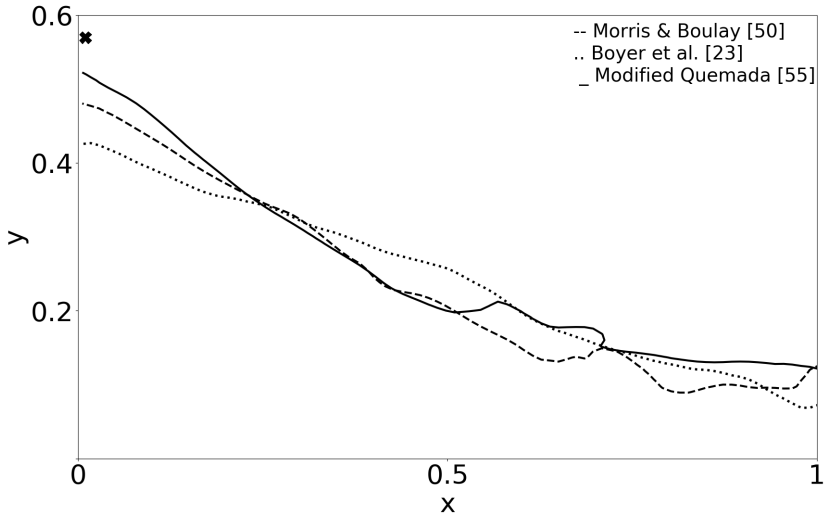


Figure 2: Final deposits using different viscosity laws. The cross symbol next to the y axis shows the height of the final deposit according to the experimental study [11].

with the modified Quemada model were more accurate than those with the other models. Further, our simulations using the modified Quemada model showed similar features of the evolution of the collapse as those recorded in the experiments of [11]. In summary, after having tested various available correlations, the one extracted from the modified Quemada model emerged as the most suitable one for the particular mixture of interest and was selected for our numerical study. The result reads,

$$\mu_{\mathrm{s}} \;=\; \mu_{\mathrm{f}} \left[\left(2.5 - \frac{2}{\phi_{\mathrm{m}}} \right) + \left(5.2 - \frac{3}{\phi_{\mathrm{m}}^2} \right) \phi_{\mathrm{s}} + \frac{\phi_{\mathrm{m}}^2}{\phi_{\mathrm{s}} \left(\phi_{\mathrm{m}} - \phi_{\mathrm{s}} \right)^2} - \frac{1}{\phi_{\mathrm{s}}} \right] . \qquad (18)$$

Finally, it is noted that the above comparison of various granular shear-viscosity correlations does not in any way imply that only shear stresses are important in the flows of interest. In particular, normal stresses and inertial force are also important and responsible for some of the unique features of granular suspensions such as particle migration in wall-bounded flows [33]; in general though, their effects are less understood than those of shear stresses.

3.2. Bulk, normal and compaction viscosities

According to the thermomechanical model in [28], the constitutive expression for the viscous stresses of the granular phase involves the shear and bulk

viscosity coefficients as well as four additional parameters. These parameters are nonlinear functions of the velocity gradients and are proportional to a third viscosity coefficient, referred to as *normal viscosity* [51]. Additionally, as mentioned above, another coefficient referred to as *compaction viscosity* enters the compaction equation (14). As explained above, and with regard to $\mu_{\rm s}$, we opted for the correlation (18) which is based on the modified Quemada model [58].

Modeling accurately ζ_s is also cumbersome due to lack of relevant experimental data. Herein we assume $\zeta_{\rm s}$ to be proportional to $\mu_{\rm s}$. This choice is motivated by the fact that ζ_s is expected to have a similar scaling behaviour with respect to $\phi_{\rm s}$; see [66] for a relevant discussion. For the sake of simplicity, the following relation is used according to [28],

$$\zeta_s \;=\; 22.5\,\mu_s\;. \tag{19}$$

Regarding the normal viscosity $\mu_{\rm n}$, only few correlations are available in the literature. Morris & Boulay [51] argued that since the divergence of both $\mu_{\rm sus}$ and $\mu_{\rm n}$ comes from particle interactions, then the normal viscosity can be assumed to diverge when $\phi_{\rm s} \to \phi_{\rm m}$ with the same asymptotic behaviour as that of $\mu_{\rm sus}$. Boyer et al. [59] also proposed a correlation for $\mu_{\rm n}$, which is very similar to that in [51]; in fact it differs from it by a proportionality coefficient only. In our study we opted for the correlation proposed in [51] which reads,

$$\mu_{\rm n} \;=\; 0.75\,\mu_{\rm f}\frac{\phi_{\rm s}}{(\phi_{\rm m}-\phi_{\rm s})^2}\;. \tag{20}$$

According to relations (12), the coefficients $\mu_{\rm s'}$, $\zeta_{\rm s'}$, χ_1 and χ_2 of equation (10) are all nonlinear functions of the strain-rate tensor $\boldsymbol{D}_{\mathbf{s}}$ and proportional to $\mu_{\rm n}$.

Finally, there is very little information in the literature about the compaction viscosity $\mu_{\rm c}$ that appears in equation (14). By analogy with migration models [35], and due to the lack of additional information, we simply set,

$$\mu_{\rm c} \;=\; \mu_{\rm f}\,. \tag{21}$$

4. Numerical results

In this section, we present results of 2D numerical simulations of the collapse of granular columns of coarse sand in water. Comparisons between

our numerical predictions and the experimental results of Thompson and Huppert [11] are also provided herein. Further, we present an analysis of the role of the initial volume fraction and the aspect ratio of the column.

4.1. Numerical setup

In our study we consider two different initial volume fractions, $\phi_{\mathrm{s,i}} = 0.554$ and $\phi_{\mathrm{s,i}} = 0.59$, that correspond to *loose* and *dense* initial packings, respectively. These values have also been used in earlier studies, [18, 26, 27], albeit for different mixtures. We also consider three different values of the aspect ratio of the column, namely, $a = 0.5$, 1.0 and 2.0. The latter value is chosen because it is the same as in the experiments [11]. The other two values have been selected on the basis of the analysis in [26] which establishes different types of collapse depending on the initial aspect ratio. More specifically, if the initial aspect ratio a is below a critical value, then part of the column will be unaffected by the collapse and the final deposit would have a trapezoidal shape. On the other hand, if $a > a_{\mathrm{cr}}$, then the whole column would be mobilized and the final deposit would attain a triangular shape. In [26], the measured critical value for loosely-packed columns of glass beads given is $a_{\mathrm{cr}} = 0.87$. Similarly, Rondon et al. [18], who carried experiments with glass beads and a mixture of water with Ucon oil, reported that $a_{\mathrm{cr}} = 0.8$ for dense packings but it decreases at loose packings. On the basis of these data, we have selected $a = 0.5$ and $a = 1.0$ with the expectation to be able to capture the two different types of collapse for the mixture in hand.

Next we provide the values of the physical parameters in our simulations. Regarding the granular phase, the grain diameter is set to $d_{\mathrm{p}} = 5.6 \times 10^{-4}$ m and the density to $\rho_{\mathrm{s}} = 2530$ kg/m^3. These values are typical of coarse sand and also match those considered in [26], thereby allowing comparison between results for columns of sand and glass beads. The maximum packing was set at $\phi_{\mathrm{m}} = 0.6$ which is a generally accepted value for sand-water mixtures. Regarding the water properties, we employ the values at 20° C; thus $\rho_{\mathrm{f}} = 1000$ kg/m^3, $\mu_{\mathrm{f}} = 8.9 \times 10^{-4}$ Pa.s and $\zeta_{\mathrm{f}} = 2.7 \times 10^{-3}$ Pa.s [67]. According to these values, the particle Stokes number is $St = 3.5$ and the density ratio $r = \sqrt{\rho_{\mathrm{s}}/\rho_{\mathrm{f}}}$ is $r = 1.6$. Thus, the cases considered herein belong to the viscous-inertial regime [16, 20].

As mentioned above, the correlation for the shear viscosity of the granular phase (18) is derived from equation (17) and the modified Quemada model for the suspension viscosity. The correlations of the other viscosity coefficients

of the solid phase are functions of μ_s and have been introduced above, in equations (19)-(21).

For the drag coefficient δ that appears in equation (13), we employ the HKL-type correlation of [39], which is known to be valid over a wide range of volume fractions and particle Reynolds number and further takes into account inertial effects. The drag coefficient is assumed to be a function of the volume fraction ϕ_s, the particle diameter d_p and the particle Reynolds number; the latter one is given in terms of d_p, ρ_f, μ_f and the amplitude of the velocity difference $\|\boldsymbol{u}_\mathrm{f} - \boldsymbol{u}_\mathrm{s}\|$. The expression of δ being too cumbersome, it is not explicitly written for the sake of economy of space.

Additionally, the parameters γ_0 and β_0 that appear in equations (15) and (16) respectively, are also material dependent and need to be assigned a numerical value. For the specific case of water-sand mixture, we set $\gamma_0 = 1.2\times10^{-4}$ N and $\beta_0 = 0.1$ Pa. These values have been calibrated according to the experiments in [42] and previously employed in [28] yielding reasonably accurate predictions. Finally, for numerical purposes and in order to avoid numerical-stability issues related to the stiffness of β_s at maximum packing, a modified version for the expression of β_s is introduced herein, which reads

$$\beta_s = \begin{cases} -\beta_0 \log\left(\frac{\phi_\mathrm{m}-\phi_\mathrm{s}}{\phi_m}\right), & \text{if } \phi_\mathrm{s} - \phi_\mathrm{s} \geq \epsilon, \\ \beta_0 \left(\frac{1}{2}\frac{\epsilon^2}{(\phi_\mathrm{m}-\phi_\mathrm{s})^2} - \log\left(\frac{\epsilon}{\phi_\mathrm{m}}\right) - \frac{1}{2}\right), & \text{if } \phi_\mathrm{m} - \phi_\mathrm{s} < \epsilon\,, \end{cases} \tag{22}$$

where ϵ is a small number. For our simulations we set $\epsilon = 10^{-6}$.

The computational domain is a rectangle of dimensions 0.9 m $\times$ 0.3 m. The granular column is also of rectangular shape, whose dimensions vary depending on the configuration of interest. However, in all cases, the column is located at the left side of the computational domain. In this study, we place a thin compacted bed to account for the layer of glued grains that is usually placed in experiments. Inside this layer, the volume fraction is set to $\phi_\mathrm{s,i} = 0.59$. From the computational point of view, this layer also allows the implementation of a no-slip boundary condition for $\boldsymbol{u}_\mathrm{s}$ at the bottom wall. The rest of the domain is assumed to be filled with water. For purposes of numerical stability, in cells with pure water, we prescribe a very small value of the solid volume fraction, $\phi_\mathrm{s} = 10^{-5}$. The other boundary conditions are the following: the right boundary is assigned an outflow (zero-Neumann) condition, the top boundary a no-slip one, and the left boundary is assumed to be a symmetry plane. The computational domain is discretized with a

uniform collocated grid consisting of 512×256 cells.

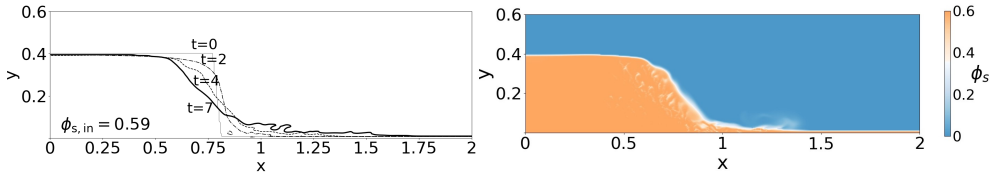
All the results discussed in subsections 4.2 and 4.3 below are given in dimensionless form. To this end, the height of the domain, $h = 0.3$ m, has been chosen as the reference length. Accordingly, the reference velocity takes the value $u_{\mathrm{ref}} = \sqrt{2\,g\,h} = 2.4$ m/s.

4.2. Collapse of densely-packed columns

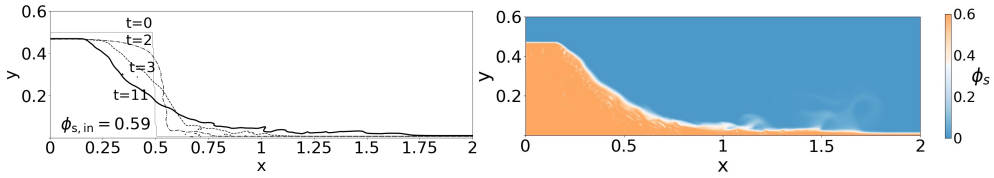
In this subsection we analyze the collapse of densely-packed columns of sand, for the three aspect ratios indicated above. As already mentioned, the initial volume fraction is set to $\phi_{\mathrm{s,i}} = 0.59$. In Figure 3, we provide plots of the profiles of the columns at various time instances. According to our simulations, the collapse always starts with the detachment and falling of the top right corner. Also, a failure line appears within the column, starting from the toe of the column and moving across the bulk. The sand from the upper right part undergoes shear and falls alongside the failure line as a single block, while the remaining part of the column slowly compacts so as to reach maximum packing. There is no visible collapse below the failure line. When $a = 2.0$, the failure line terminates at the left lateral boundary of the column without ever reaching its top boundary. However, for $a = 0.5$ and $a = 1.0$, the failure line intersects the top boundary of the column in the early stages of the collapse; accordingly, the final deposit is of trapezoidal shape. For those aspect ratios, a large part of the column (the one below the failure line) remains unaffected by the collapse and compacts only slightly. A video animation of the simulation of the collapse of the densely-packed column with $a = 2.0$ is provided as supplementary material and illustrates further the various aspects of the collapse.

colour-filled plots of the final distribution of ϕ_{s} are also shown in Figure 3, so as to better visualize the final deposit (remnant pile) of sand, which is a trapezoid for $a = 0.5$ and $a = 1.0$ and a triangle for $a = 2$. In other words, there is a critical aspect ratio for densely-packed columns above which the shape of the final deposit changes from trapezoidal to triangular. In the experimental study [18] it was reported that the final deposit was also trapezoidal when $a = 0.5$ but triangular for $a = 1$ and above. However, as mentioned above, those experiments involved glass beads of smaller diameter and a mixture of water and Ucon oil.

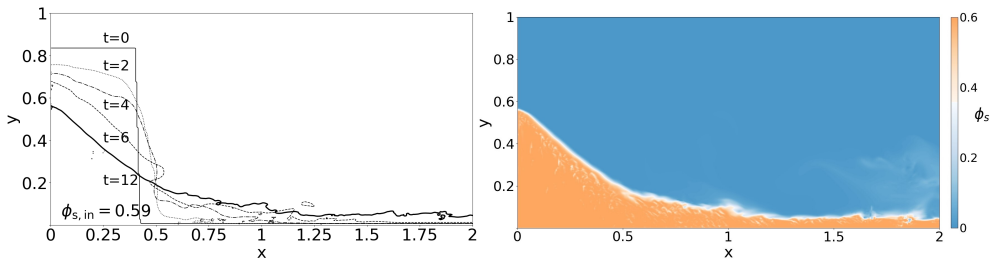
For the case $a = 2.0$, in Figure 4 we present colour-filled plots of ϕ_{s} at different time instances juxtaposed with photographs from the experiments of Thompson and Huppert [11]. We can infer that the features of the collapse,



(a) Aspect ratio $a = 0.5$



(b) Aspect ratio $a = 1.0$



(c) Aspect ratio $a = 2.0$

Figure 3: Evolution of the column profile over time (left) and final deposits (right) for densely-packed columns of different aspect ratios.

as predicted by the simulations, are in reasonable agreement with the ones observed in the experiments. As mentioned above, the top right (respectively, left) corner of the column in the simulation (respectively, experiment) starts to fall as a block along a failure line. Then, the part of the column above the failure line collapses, while the rest starts to compact. The final deposit is composed of the sand below the failure line and assumes a triangular shape.

Regarding the angle of repose θ, our simulation predicted $\theta = 36^\circ$ which compares satisfactorily with the experimental result $\theta = 32^\circ$ in [11]. A relevant useful quantity is the (dimensionless) runout distance L_∞. This is defined as $L_\infty = (L_\mathrm{f} - L_\mathrm{i})/L_\mathrm{i}$, where L_i and L_f are the lengths of the initial column and final deposit, respectively. Our numerical prediction is $L_\infty = 1.4$, which agrees reasonably well with the experimental value $L_\infty = 1.8$ of [11]. It should also be noted that both θ and L_∞ depend on the initial packing; however its value in the experiments is not provided in [11].

In the two other cases with smaller aspect ratios, the numerical predic-

tions for the angle of repose are similar to that for $a = 2.0$. More specifically, for $a = 1.0$ and 0.5 our predictions for the runout distance are $L_\infty = 0.8$ and $L_\infty = 0.4$, respectively. On the other hand, the angle of repose is found to be $\theta \approx 40^\circ$ for both of these aspect ratios.

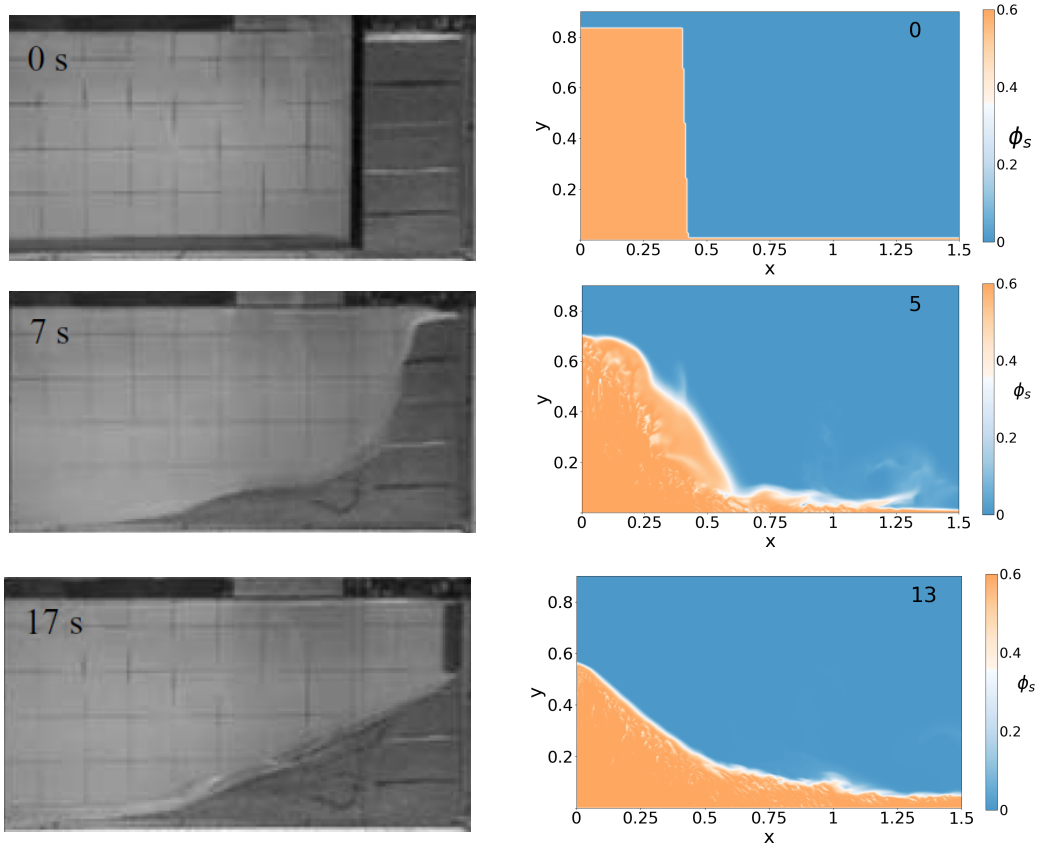


Figure 4: Collapse of densely-packed columns. Comparison between the experiments of Thompson and Huppert [11] (left) and our simulation for aspect ratio $a = 2.0$.

Another quantity of interest is the ratio between the final and initial height, $\frac{H_\mathrm{f}}{H_\mathrm{i}}$. From the results of [11] it can be inferred $\frac{H_\mathrm{f}}{H_\mathrm{i}} \approx 0.76$ while our numerical prediction was approximately equal 0.71, which shows once again good agreement between simulations and experiments. These results suggest that when the aspect ratio increases, the final-to-initial height ratio drops substantially. This drop can be explained by the fact that, at high aspect ratios, the failure line passes through the bulk of the column and terminates

at its left boundary without ever reaching the top. Therefore, the entire upper part of the column (including the top left corner) is mobilized and falls along that failure line, thereby resulting in a lower final height. By contrast, at smaller aspect ratios, the failure line does not terminate at the left boundary of the pile but at its top boundary. Accordingly, there is a part of the top side of the column that remains intact and, consequently, the final height stays close to the initial one. Accordingly, and since the repose angle does not vary a lot, the runout distance also decreases with the aspect ratio.

Regarding the final-to-inital height ratio for $a = 2$, a similar value was measured by Rondon et al. [18], namely $\frac{H_\mathrm{f}}{H_\mathrm{i}} \approx 0.7$, even though their experiments involved different materials. However, there are differences in the values of the runout distance L_∞. While our simulation predicts $L_\infty = 1.4$, Rondon et al. [18] measured a runout distance $L_\infty \approx 3$ for their mixture. The larger experimental value is apparently due to the fact that the motion of glass beads is less dissipative than that of sand.

Next, in Figure 5, we present plots of the evolution of the normalized runout distance, λ, with time. This quantity is defined as $\lambda = \frac{L(t)-L_\mathrm{i}}{L_\mathrm{f}-L_\mathrm{i}}$, where $L(t)$ is the position of the front at a given time. In this figure, the evolution of λ is presented in terms of the normalized time, t/t_f, with t_f being the time instance that the collapse is completed. We readily observe that the plots for the three different aspect ratios are very close to one another and, furthermore, their shape is similar to a sigmoid curve. Accordingly, the evolution of the runout distance can be divided in three different phases. In the first phase, until $t/t_\mathrm{f} \approx 0.15$, the propagation velocity of the front is moderate, *i.e.* λ increases moderately with time. In the next phase, which lasts until $t/t_\mathrm{f} \approx 0.75$, the front velocity is substantial. This is the phase during which most of the material leaves the column and gets mobilized. Finally, in the third phase, the front decelerates as the collapse approaches completion and its velocity eventually becomes zero.

The differences between the plots of Figure 5 is attributed, to a certain extent, to the inherent imprecision in determining the instantaneous location of the front. More specifically, in order to avoid slip at the bottom wall, in our simulations we introduce a horizontal bed of sand which has a small but finite thickness. As the material from the column falls down and propagates downstream, it interacts with this bed and mobilizes a small part of it, which sometimes renders cumbersome the determination of the exact location of the

front. By contrast, in experiments one uses a single layer of glued particles and is therefore not confronted with this problem.

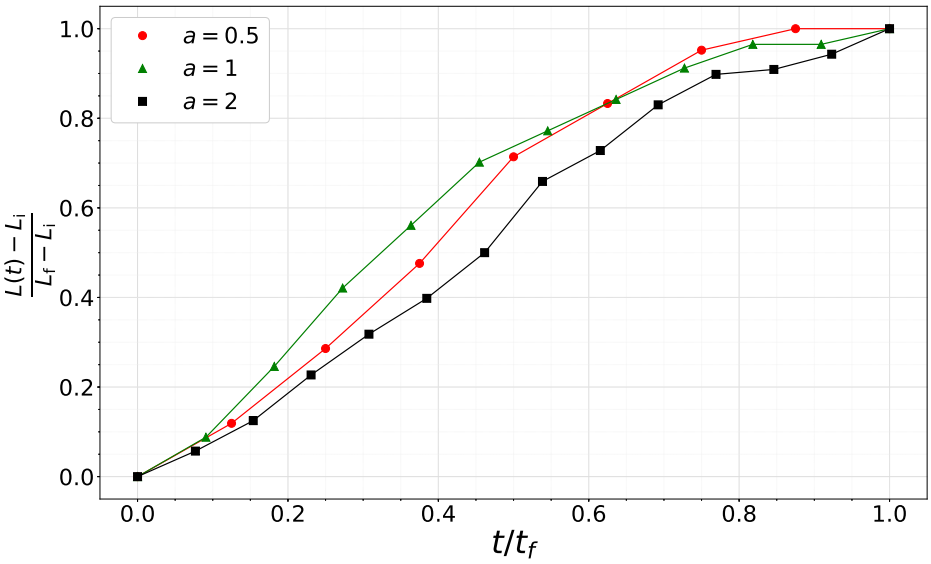


Figure 5: Evolution of the normalized runout distance over time for three different aspect ratios a in the case of densely-packed columns.

Further, on the basis of the results shown in Figures 3 and 4, we infer that, for dense initial packing, the size of the remnant piles is comparable to that of the initial columns. Moreover, for the range of aspect ratios considered herein, the collapsing part of the column does not flow but instead crawls above the failure line. This behaviour has been observed in earlier experiments with different materials [15, 18] and is typical of densely-packed columns. Its explanation is as follows. Dense columns have to dilate first and relax the grain-to-grain interactions in order to attain a microstructural state that allows them to start flowing. While dilating, the gaps between grains are filled by the fluid which is therefore being sucked in the column. This phenomenon is known as *pore-pressure feedback* [15, 18]. This dilation process tends to stabilize the column and prevents it from flowing instantaneously like a viscous liquid. Consequently, the amount of fluid set in motion is considerably smaller than what one would expect on the basis of the weight of column above the failure line.

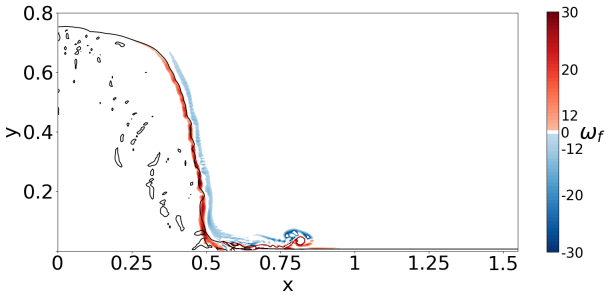
This observation is corroborated by the vorticity plots shown in Figure 6. In these plots we can observe that initially a pair vortices is formed at the toe of the column and is advected downstream. However, these vortices have small size and low intensity, and apparently they do not play an important role in the process of the collapse. During the collapse, additional vortices are formed at the toe and along the slope which carry entrained sand grains. Overall, the collapsing material pushes the water adjacent to the toe of the column but does not induce a particularly strong current. As the column slowly reaches its final state, the vortical structures diffuse and their strength drops significantly.

Therefore, in densely-packed columns, the amount of suspended sand is expected to be relatively small. This can be confirmed by the plots of the amount of suspended sand over time that are shown in Figure 7. For $a = 0.5$ and $a = 1.0$, in which the collapse produces a trapezoidal remnant pile, the amount of transported sand is quite small: 2.8% and 5.8%, respectively, of the initial mass of the column. This is explained by the fact that most of the collapsing material settles in the vicinity of the foot of the initial column. In fact, the spreading of the front of dense columns is found to be almost half than the value for loosely-packed columns reported in [18].

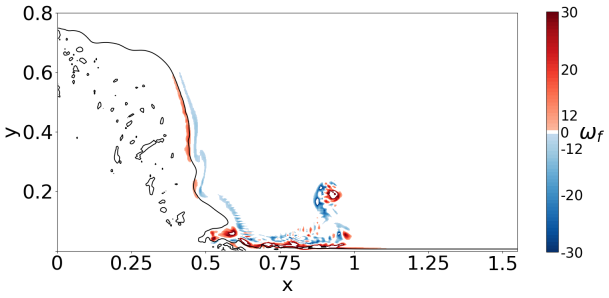
In the case of the high aspect ratio, $a = 2.0$, the amount of suspended sand at the end of the process is also relatively small. It is equal to 11% of the mass of the initial column, which is nonetheless proportionally higher than in the previous cases. This is explained by the fact that in this case the entire upper side of the column is mobilized, which allows for the suspension of higher amounts of sand. Some of this material is entrained in the vortices mentioned above and is transported away. It is also interesting to note that, according to Figure 7, the amount of suspended sand increases monotonically until it reaches a peak before the completion of the collapse. Beyond the peak, it drops as the suspended sand starts to settle. Interestingly, the settling of the suspended sand is a faster process than the compaction of the column below the failure line. In particular, the suspended sand has already been deposited before the compaction of the column terminates.

4.3. Collapse of loosely-packed columns

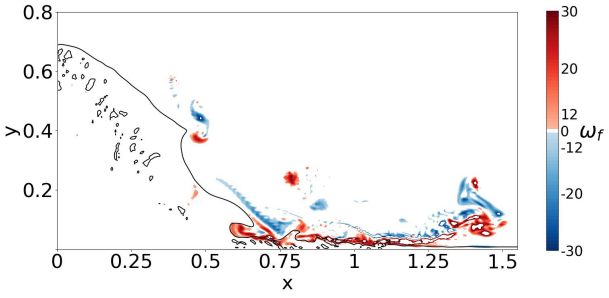
This subsection is concerned with the characteristics of the collapse of loosely-packed columns. The initial volume fraction is set at $\phi_{\mathrm{s,i}} = 0.554$. We consider the same aspect ratios as in the previous case, namely $a = 0.5$, 1.0 and 2.0. Plots of the column profiles at different time instances are



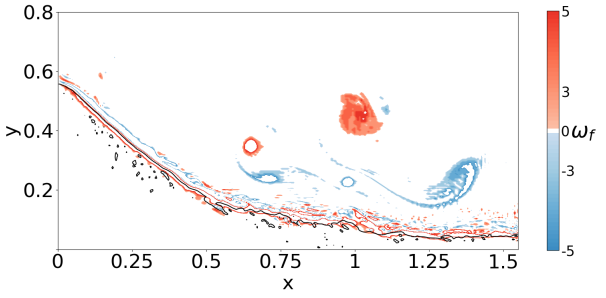
(a) t = 2



(b) t = 3



(c) t = 5



(d) t = 13

Figure 6: Vorticity distribution of the fluid phase, ω_{f}, during the collapse of a densely-packed column with aspect ratio $a = 2.0$.

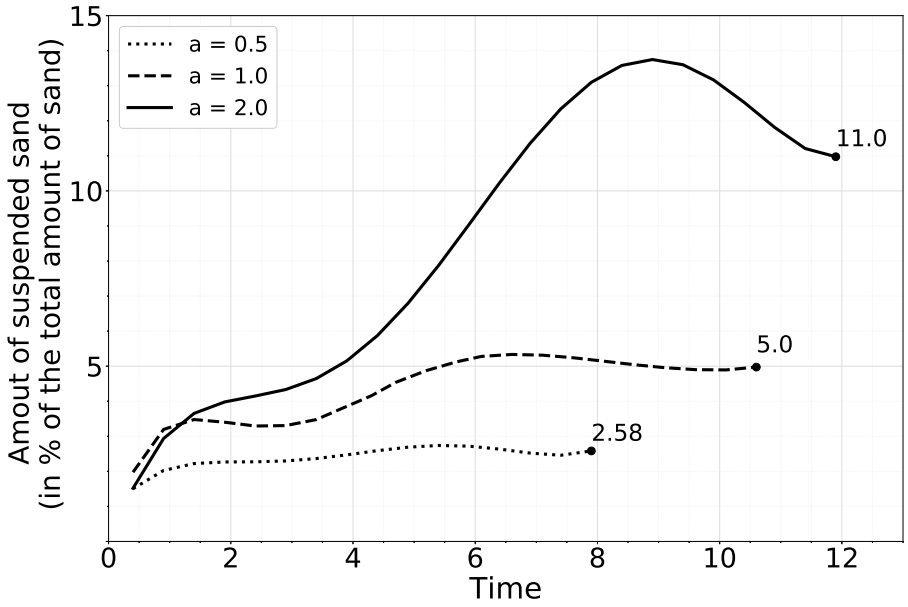
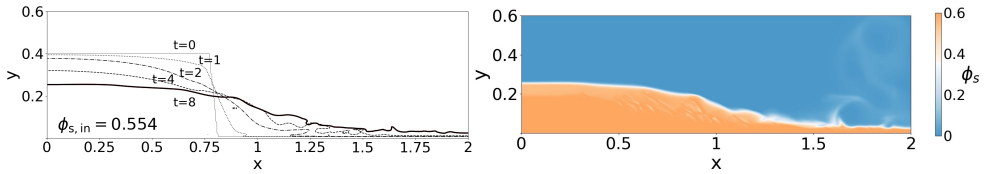


Figure 7: Amount of suspended sand over time for densely-packed columns, as percentage of the total amount of sand.

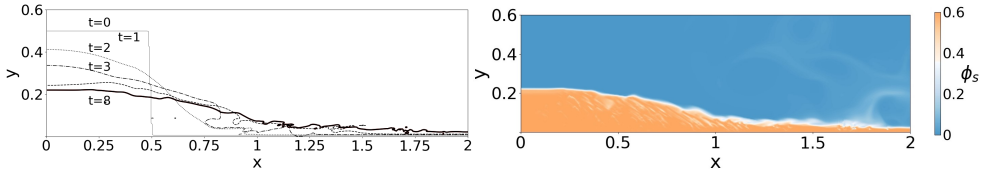
shown in Figure 8. From these plots we readily infer that the final deposit is a trapezoid for all aspect ratios, while the height of the final deposit varies only slightly with a. In other words, with regard to the shape of the final deposit, the initial aspect ratio does not seem to play a major role, at least in the range of values examined herein.

With regard to the process of the collapse, our simulations predict that the entire right side starts to fall while at the same time the column descends and compacts due to its own weight. As it can be inferred from the top part of the columns profiles in Figure 8, the compaction is rapid during the early stages of the collapse but then slows down as the volume fraction approaches the value of maximum packing. This slow-down occurs at $t \approx 4$ for all aspect ratios examined herein, which indicates that compaction is controlled mainly by the weight of the column and the initial volume fraction.

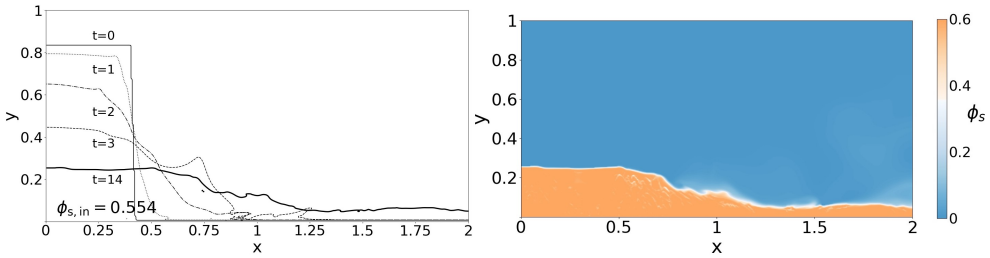
The distribution of the solid volume fraction at different time instances is plotted in Figure 9. According to it, initially the spreading of sand onto the bed is very rapid while a considerable amount of sand is transported away from the initial column. This is attributed to the rapid collapse of the right side of the column. However, as time advances, the spreading and transport



(a) Aspect ratio $a = 0.5$



(b) Aspect ratio $a = 1.0$



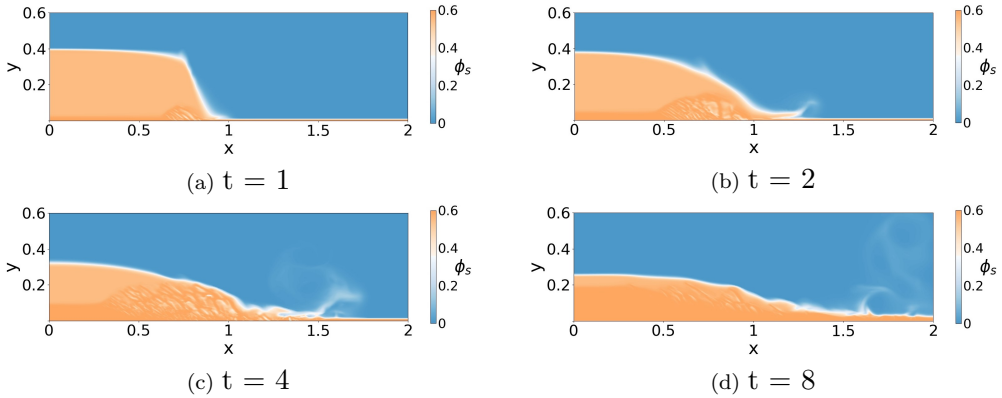
(c) Aspect ratio $a = 2.0$

Figure 8: Evolution of the column profiles during the collapse of loosely-packed columns with different aspect ratios a.

rate of sand slow down. The fast spreading of the front of loosely-packed columns was also observed experimentally in [18]. During the collapse, energy is dissipated both via hydrodynamic interactions and viscous stresses; see also the discussion [22]. Animation of the simulation of the collapse of the loosely-packed column with $a = 2.0$ is provided as supplementary material and illustrate further the various aspects of the collapse.

With regard to the angle of repose, the values predicted by our simulations for the different aspect ratios are quite close. In particular, for $a = 1.0$ and $a = 2.0$ we obtain $\theta \approx 15^\circ$ while for $a = 0.5$ the predicted value is slightly higher, $\theta \approx 19^\circ$.

As in the case of densely packed columns, while the angle of repose is only weakly influenced by the aspect ratio, the runout distance increases significantly with a. Indeed, our predictions are $L_\infty = 0.63$ for $a = 0.5$, but then $L_\infty = 2$ for $a = 1.0$ and $L_\infty = 2.5$ for $a = 2.0$ respectively. Past numerical [24, 26] and experimental [11, 18, 26, 30] results provide ample



(a) t = 1 (b) t = 2

(c) t = 4 (d) t = 8

Figure 9: colour-filled plots of solid volume fraction ϕ_s at different instances during the collapse of a loosely-packed column with aspect ratio $a = 0.5$. The evolution of ϕ_s depicts clearly the spreading and compaction of sand during the collapse.

evidence of this trend regardless of the materials that comprise the mixture. For initially dense packings of glass beads immersed in a Ucon/water mixture, both Bougouin et al. [30] and Rondon et al. [18] reported that when the aspect ratio is increased by a factor of 4, from $a = 0.5$ to $a = 2.0$, the runout distance increases approximately by the same factor. Our simulations predicted a similar factor of increase of L_∞ in sand/water mixtures.

On the other hand, the final-to-initial height ratio decreases with the aspect ratio. In particular, the predicted values for $a = 0.5$, 1.0 and 2.0 are $\frac{H_f}{H_i} \approx 0.63$, 0.44 and 0.3, respectively. To our knowledge, there are no experimental data on the collapse of loosely-packed columns of sand in water to corroborate these predictions. Nonetheless, they differ from the experiments [26] with glass beads. More specifically, for $a = 0.5$ they reported that $\frac{H_f}{H_i} = 1$ and that the final deposit is of triangular shape instead of trapezoidal. Similarly, in the experimental study [18] with glass beads, it is reported that the final deposit was triangular for all three aspect ratios considered herein. This difference may be attributed to the fact that glass beads and sand have different rheological behaviour. Further, the experiments [18] and [26] involved smaller columns than the ones assumed herein and this can also contribute to the observed differences. Actually, recent numerical studies [29] indicate that the size of the column contributes to the shape of the final deposit. Nevertheless, in [18] it is reported that $\frac{H_f}{H_i} = 0.5$ when $a = 0.67$, which is compatible with our numerical predictions.

Next, we examine the fluid motion and the emerging vortical structures.

As the column collapses, the falling sand pushes the surrounding water and sets it in motion. Fluid is expected to be expelled from the pores due to the pore-pressure feedback for loosely-packed columns [15, 19]. According to this phenomenon, grains tend to get closer to one another as the column undergoes compaction and force the fluid out of it, which also contributes to the formation of vortices. In Figure 10 we present colour-filled plots of the vorticity fluid at different time instances for the case $a = 2$. Therein it can be observed that the vortices formed along the slope and at the toe of the column are advected downstream and interact with each other. Grains are also entrained in the vortices, which increases the amount of suspended sand. From Figure 10, we infer that the induced fluid motion is more intense than in densely-packed columns. Strong vortical structures have also been predicted in the computations of Lee et al. [26] with glass beads. According to our simulations the generated vortical structures are advected downstream even after the completion of the collapse. Evidently, with a more viscous fluid, the vortices would diffuse faster than in our case [19, 31].

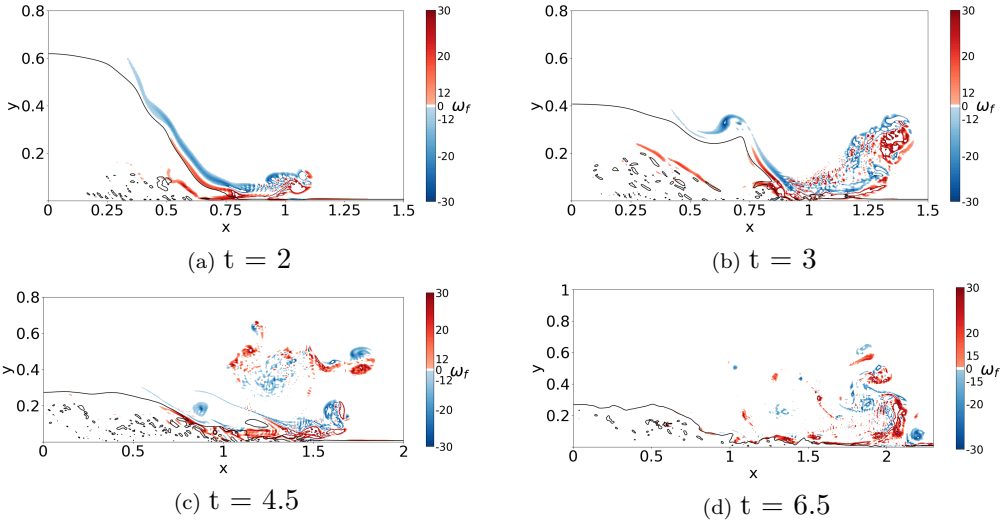


Figure 10: Vorticity distribution of the fluid phase, ω_f during the collapse of a loosely-packed column of aspect ratio $a = 2$.

With regard to the transport of sand, upon comparison of Figures 3 and 8, we see that the horizontal bed in loosely-packed columns is always thicker than in densely-packed ones, regardless of the initial aspect ratio. In other words, the amount of transported sand always increases as the initial packing

decreases, as expected. In general, sand is transported away from the column via two mechanisms: i) gravity-induced displacement and direct deposition, and ii) transport of suspended grains by the water and subsequent settling.

In Figure 11 we have plotted the temporal evolution of the amount of suspended sand for loosely-packed columns. As in densely-packed ones, this amount increases monotonically with the aspect ratio. This can be explained by the fact that as a increases, the initial potential energy is higher and therefore, there will be a higher amount of potential energy converted to kinetic one. Radjai et al. [68] mentioned that during the collapse of the vertical side, the initial potential energy is dissipated via contact interactions between grains and interphasial drag. However, in the case of loosely-packed columns, there is more space between the grains and therefore less dissipation via contact interactions. As a result, the grains of the collapsing part carry more kinetic energy, which makes it easier for them to get suspended. In other words, the granular viscous stresses decrease with ϕ_s, as is evident from the constitutive law (10) for $\boldsymbol{\tau}_s$ and the correlation (18) for μ_s.

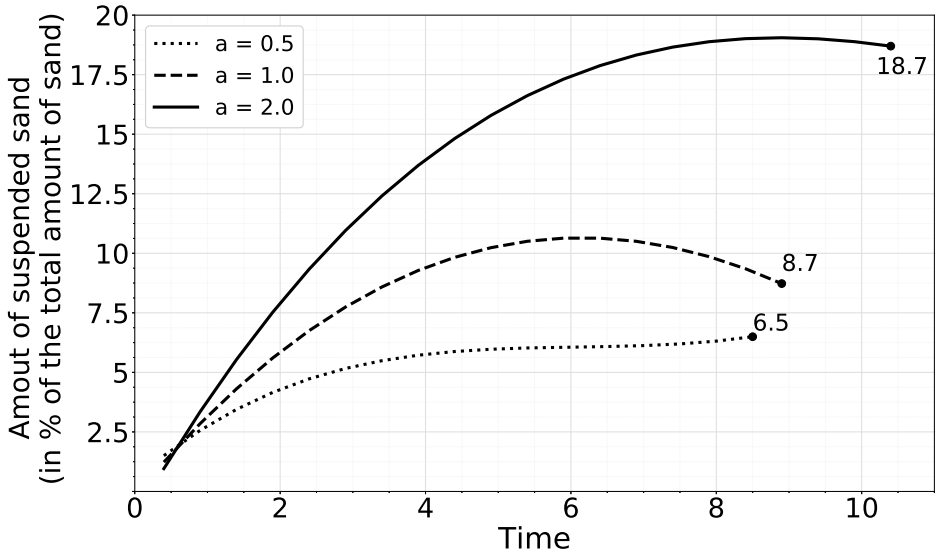


Figure 11: Evolution of the amount of suspended sand with time for loosely-packed columns, in percentage of the total mass of sand in the initial column.

Finally, for comparison purposes, in Table 2 we provide the maximum amount of suspended sand, as percentage of the total amount of sand, for

all the cases examined herein. We confirm that, for all aspect ratios, the amount of suspended sand increases significantly as the initial packing becomes more loose. However, this difference gets smaller as the initial aspect ratio increases. This can be explained by the fact that for densely-packed columns with high aspect ratios, the failure line reaches the left boundary so that the entire upper side of the column is mobilized, thereby leading to increased amount of suspended sand.

	$\phi_{\mathrm{s,i}} = 0.59$	$\phi_{\mathrm{s,i}} = 0.554$
a=0.5	2.8%	6.5%
a=1.0	5.8%	10.8%
a=2.0	13.8%	19.1%

Table 2: Maximum amount of suspended sand, in percentage of the total amount of sand present in the final stage of collapse

5. Further discussion on the runout distance and the final height

In this section, we discuss further our numerical predictions for the final height and runout distance. As mentioned previously, results in the literature involving a mixture of water and sand are particularly scarce. For this reason, our results are herein compared to those of earlier experimental and numerical studies, using different mixtures. Additionally, the influence of the fluid viscosity on the runout distance is examined via a parametric study, the results of which are provided in the second part of this section.

5.1. Comparisons of runout distance and final height

In Figure 12 we have plotted the dimensionless runout distance L_∞ against the aspect ratio for densely and loosely-packed columns, as well as for columns with an intermediate initial packing $\phi_{\mathrm{s,i}} = 0.57$. We can observe that L_∞ increases almost linearly with the aspect ratio a. Furthermore, the increase rate is more pronounced at loose packings, (*i.e.* it gets higher as $\phi_{\mathrm{s,i}}$ decreases. With regard to comparisons with earlier studies, our numerical prediction is close to the experimental result of [11] for sand columns immersed in water. Further, according to Figure 12, our predictions are in good agreement with those of [26] for mixtures of glass beads and water. On the other hand,

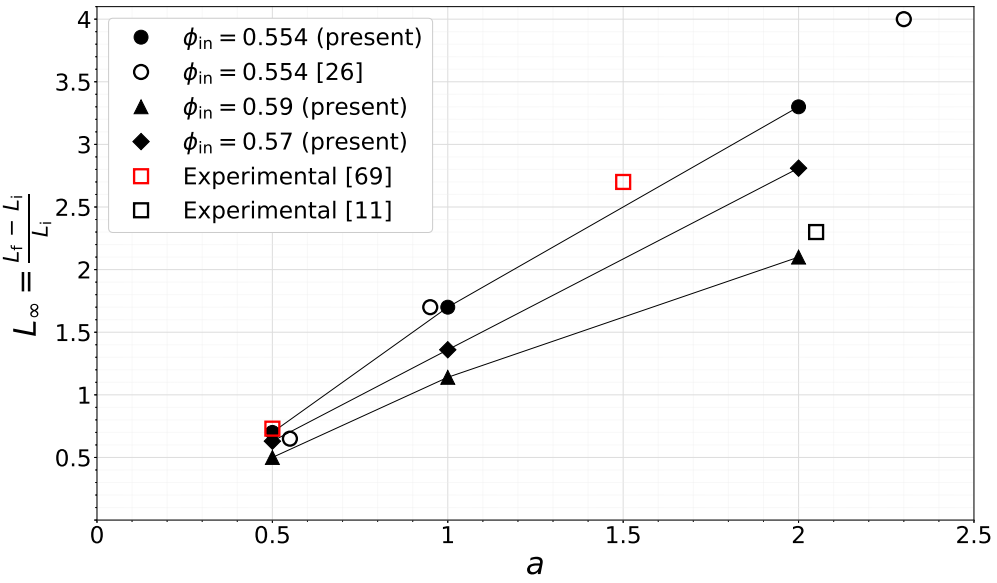


Figure 12: Dimensionless runout distance, L_∞, for different aspect ratios a and initial volume fractions $\phi_{s,i}$. The experiments [11] used a sand and water. On the other hand, the authors of [26, 69] considered glass beads immersed in water, while the authors of [18] considered glass beads immersed in a mixture of water and Ucon oil.

there is some discrepancy with the experimental result [69], which was also conducted with glass beads and water.

In Figure 13 we have plotted our numerical results for the ratio between final height and initial length of the columns, $\frac{H_f}{L_i}$, juxtaposed with those from earlier investigations. According to our simulations, this ratio increases monotonically with the aspect ratio a; however the rate of increase is not the same for all initial packings. For loosely-packed columns it increases only slightly over the range of a considered herein, and in a linear fashion. Densely-packed columns exhibit the opposite behaviour; the increase rate of $\frac{H_f}{L_i}$ is significant for $a < 1$ but then it becomes less pronounced for $a > 1$. The results for the intermediate initial packing $\phi_{s,i} = 0.57$ have a trend that is closer to that of densely-packed columns, albeit the rate of increase of $\frac{H_f}{L_i}$ for $a < 1$ is less pronounced.

Regarding comparisons with earlier studies, our results for loosely-packed columns are in relatively good agreement with the experiments [18] for glass beads immersed in a mixture of water and Ucon oil. However there are

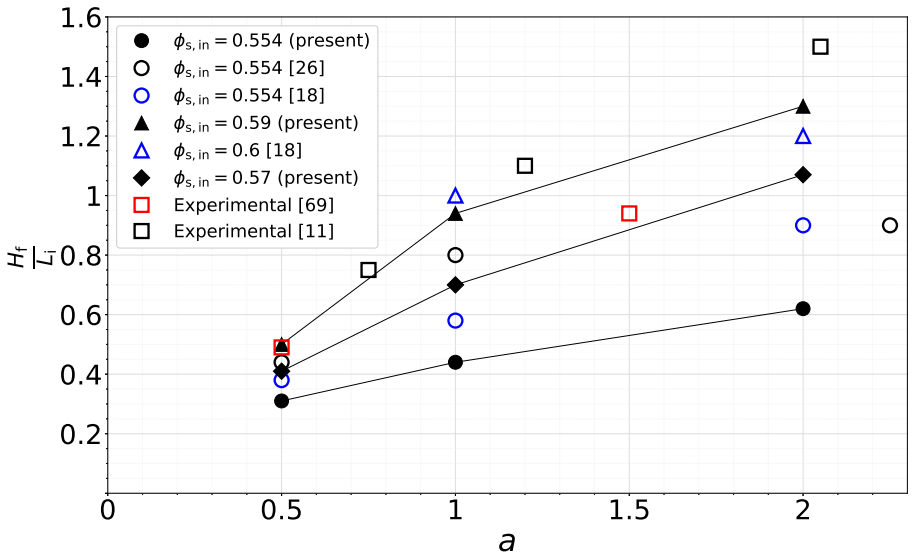


Figure 13: Values of the ratio between final height and initial length, $\frac{H_f}{L_i}$, for different aspect ratios a and initial volume fractions $\phi_{s,i}$.

some discrepancies with the numerical results of [26], especially when $a = 1$. These can be attributed to the different size of granular columns; in [26] it was smaller by an order of magnitude than in our case. Such discrepancies have been previously reported in [29] regarding predictions of final heights when considering columns of different dimensions, especially for loose packings. Also, the difference in the materials between [26] and in our study also contributes to the observed discrepancies. For densely-packed columns, we also report good agreement with the experiments in [11], [18] and [69]. It is worth adding that those experimental studies did not report the value of the initial packing; however, based on the final deposits it is reasonable to assume that they used densely packed columns.

5.2. Effect of the viscosity on the runout distance

Finally, we investigate the influence of the viscosity on the runout distance L_∞. To this end, the viscosity of the fluid is varied over several decades, with a corresponding variation of the Stokes number St. Herein we employ the

following definition of St, [20, 24],

$$St \;=\; \frac{1}{18\sqrt{2}} \frac{\left(\rho_{\mathrm{s}}\, \Delta\rho\, g\, d^3\right)^{1/2}}{\mu_{\mathrm{f}}}\,, \tag{23}$$

where $\Delta\rho$ is the difference between the densities of the two phases.

The results are shown in Figure 14, juxtaposed with the experimental data [20] and numerical results [24]. According to them, the runout distance increases monotonically with St, i.e. as the fluid viscosity decreases. This lower fluid viscosity implies lower drag forces acing on the particles. Further, according to Figure 14, the plot of L_∞ can also be approximated by a sigmoid curve. In particular, for $1 < St < 4$, the increase rate of L_∞ is rather mild but it becomes much steeper for $4 < St < 10$. Then, for $St > 10$ the increase rate drops and eventually L_∞ reaches a plateau of $L_\infty \approx 1.1$ at $St = 50$.

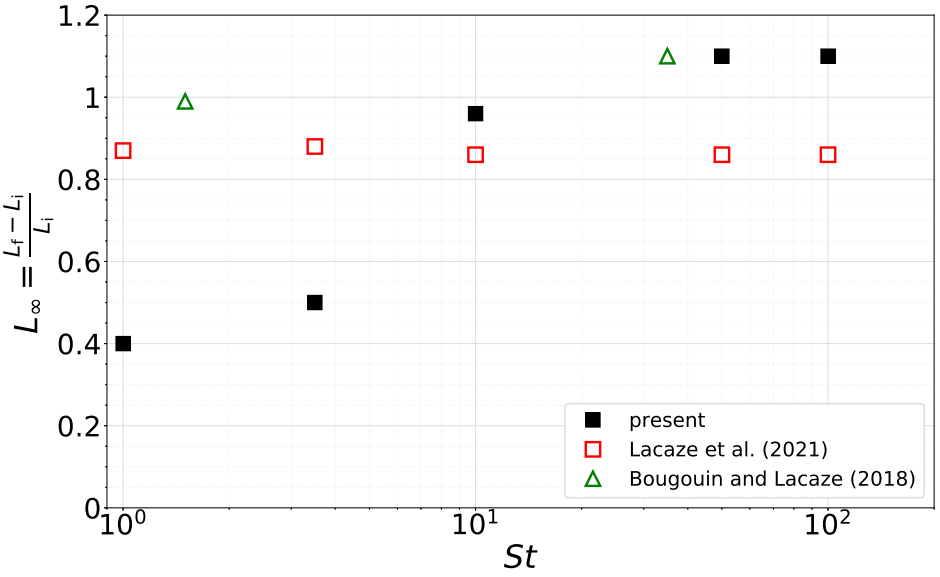


Figure 14: Variation of (dimensionless) runout distance with the fluid viscosity (expressed in terms of the Stokes number).

For $St \geq 10$, our results are in reasonably good agreement with both experimental and numerical results of [20] and [24]. On the other hand, at lower St, the discrepancies become significant. Interestingly, though, the numerical; study of [24] also predicted an S-shaped variation of the runout

distance with St; however, the part of the steep increase of L_∞ occurred at a lower range of St than in our study.

6. Conclusions

In this paper, we presented a numerical study of the collapse of a column of coarse sand immersed in water. Our simulations were based on a two-velocity, two-pressure continuum model that also incorporates nonlinear rheology modeling and an evolution equation for the solid volume fraction. With regard to the granular shear viscosity, we tested various correlations that we extracted from earlier models for the mixture viscosity. These tests revealed that the correlations based on the modified Quemada model [58] gave better comparisons with experiments for the mixture in hand.

In our simulations we considered both densely and loosely-packed columns at different aspect ratios, namely $a = 0.5$, 1.0 and 2.0. Our results for dense packings and $a = 2.0$ showed good agreement with the experiments [11], regarding both the evolutions of the collapse and the geometry of the final deposit. It was confirmed that the direction of the failure line determines the shape of the final deposit. If it intersects the upper side of the column, then the final deposit is a trapezoid; otherwise, it intersects the lateral side and the final deposit is a triangle. In densely-packed columns, the collapse always starts with the detachment and falling of the top corner. Then, the collapsing material moves downhill along the failure line, almost as a single block. The final deposit is trapezoidal for the small and intermediate aspect ratios and triangular for the high one. On the contrary, in loosely-packed columns the entire lateral side falls while at the same time the column descends and compacts due to its own weight. Also, the motion of the falling material is more fluid-like, as expected. The final deposit of loosely-packed columns is trapezoidal for all three aspect ratios considered herein.

Further, our simulations predicted that the runout distance L_∞ increases linearly with the aspect ratio a. The rate of increase is slightly more higher at lower packings. The ratio $\frac{H_\mathrm{f}}{L_\mathrm{i}}$ also increases with a. Overall, our numerical predictions of these two quantities compare satisfactory with date from earlier experimental and numerical studies, that were nonetheless conducted with different materials. Moreover, the amount of suspended and transported sand depend on both the initial packing and the aspect ratio; more specifically it increases with the aspect ratio while it decreases when the volume fraction.

In terms of future directions, since the process of collapse is different in densely and loosely packed columns, it is worth investigating via parametric studies whether there is a critical initial volume fraction $\phi_{s,i}$ that marks the transition from one type of collapse to the other or if this transition occurs gradually with varying $\phi_{s,i}$. Moreover, it is interesting to study the effect of the particle diameter and the actual size of the column, not only on the shape of the final deposit but also on the overall dynamics of the collapse and the induced particle-laden flow.

References

[1] B. Andreotti, Y. Forterre, O. Pouliquen, Granular Media: Between Fluid and Solid, Cambridge University Press, 2013.

[2] P. Richard, M. Nicodemi, R. Delannay, P. R. D. Bideau, Slow relaxation and compaction of granular systems, Nature Mater. 4 (2005) 121–128.

[3] G. Lube, H. Huppert, R. Sparks, M. Hallworth, Axisymmetric collapses of granular columns, J. Fluid Mech. 508 (2004) 175–199.

[4] E. Lajeunesse, A. Mangeney-Castelnau, J. P. Vilotte, Spreading of a granular mass on a horizontal plane, Phys. Fluids 16 (2004) 2371.

[5] N. J. Balmforth, R. R. Kerswell, Granular collapse in two dimensions, J. Fluid Mech. 538 (2005) 399–428.

[6] L. Lacaze, J. C. Phillips, R. R. Kerswell, Planar collapse of a granular column: Experiments and discrete element simulations, Phys. Fluids 20 (2008) 063302.

[7] B. J. Konijn, O. B. J. Sanderink, N. P. Kruyt, Experimental study of the viscosity of suspensions: Effect of solid fraction, particle size and suspending liquid, Powder Tech. 266 (2014) 61–69.

[8] M. Cabrera, N. Estrada, Granular column collapse: Analysis of grain-size effects, Phys. Rev. E 99 (2019) 012905.

[9] P.-Y. Lagrée, L. Staron, S. Popinet, The granular column collapse as a continuum: validity of a two–dimensional Navier–Stokes model with a μ(I)–rheology, J. Fluid Mech. 686 (2011) 378–408.

[10] L. Staron, E. J. Hinch, Study of the collapse of granular columns using two-dimensional discrete-grain simulation, J. Fluid Mech. 545 (2005) 1–27.

[11] E. Thompson, H. Huppert, Granular column collapses: further experimental results, J. Fluid Mech. 575 (2007) 177–186.

[12] P. Si, H. Shi, X. Yu, Development of a mathematical model for submarine granular flows, Phys. Fluids 30 (2018) 083302.

[13] C. Meruane, A. Tamburrino, O. Roche, On the role of the ambient fluid on gravitational granular flow dynamics, J. Fluid Mech. 648 (2009) 381–404.

[14] V. Topin, Y. Monerie, F. Perales, F. Radjaï, Collapse dynamics and runout of dense granular materials in a fluid, Phys. Rev. Lett. 109 (2012) pp.188001.

[15] R. M. Iverson, Regulation of landslide motion by dilatancy and pore pressure feedback, J. Geophys. Res. Atmos. 110 (2005).

[16] C. Cassar, M. Nicolas, O. Pouliquen, Submarine granular flows down inclined planes, Phys. Fluids 17 (2005) 103301.

[17] M. Pailha, M. Nicolas, O. Pouliquen, Initiation of underwater granular avalanches: Influence of the initial volume fracton, Phys. Fluids 20 (2008) 111701.

[18] L. Rondon, O. Pouliquen, P. Aussillous, Granular collapse in a fluid: role of the initial volume fraction, Phys. Fluids 23 (2011) 073301.

[19] C. Wang, Y. Wang, C. Peng, X. Meng, Dilatancy and compaction effects on the submerged granular column collapse, Phys. Fluids 29 (2017) 103307.

[20] A. Bougouin, L. Lacaze, Granular collapse in a fluid: Different flow regimes for an initially dense-packing, Phys. Rev. Fluids 3 (2018) 064305.

[21] G. Pinzon, M. Cabrera, Planar collapse of a submerged granular column, Phys. Fluids 31 (2019) 086603.

[22] L. Jing, G. C. Yang, C. Y. Kwok, Y. D. Sobral, Dynamics and scaling laws of underwater granular collapse with varying aspect ratios, Phys. Rev. E 98 (2018) 042901.

[23] S. Gallier, E. Lemaire, F. Peters, L. Lobry, Rheology of sheared suspensions of rough frictional particles, J. Fluid Mech. 757 (2014) pp. 514–549.

[24] L. Lacaze, J. Bouteloup, B. Fry, E. Izard, Immersed granular collapse: from viscous to free-fall unsteady granular flows, J. Fluid Mech. 912 (2021) A15.

[25] F. Boyer, O. Pouliquen, E. Guazzelli, Dense suspensions in rotating-rod flows: normal stresses and particle migration, J. Fluid Mech. 686 (2011) 5–25.

[26] C.-H. Lee, Z. Huang, M.-L. Yu, Collapse of submerged granular columns in loose packing: Experiment and two-phase flow simulation, Phys. Fluids 30 (2018) 123307.

[27] C.-H. Lee, Z. Huang, A two-phase flow model for submarine granular flows: With an application to collapse of deeply-submerged granular columns, Adv. Water Res. 115 (2018) 286–300.

[28] D. Monsorno, A. A. Dimas, M. V. Papalexandris, Time-accurate calculation of two phase granular flows exhibiting compaction, dilatancy and nonlinear rheology, J. Comput. Phys. 372 (2018) 799–822.

[29] A. Busch, S. Johansen, On the validity of the two-fluid-KTGF approach for dense gravity-driven granular flows as implemented in ANSYS Fluent R17.2, Powder Tech. 364 (20) 429–456.

[30] A. Bougouin, L. Lacaze, T. Bonometti, Collapse of a liquid-saturated column on a horizontal plane, Phys. Rev. Fluids 4 (2019) 124306.

[31] S. Courrech du Pont, P. Gondret, B. Perrin, M. Rabaud, Granular avalanches in fluids, Phys. Rev. Lett. 90 (2003) 044301.

[32] D. Monsorno, C. Varsakelis, M. V. Papalexandris, A thermomechanical model for granular suspensions, J. Fluid Mech. 808 (2016) 410–440.

[33] D. Monsorno, C. Varsakelis, M. V. Papalexandris, Poiseuille flow of dense non-colloidal suspensions: the role of intergranular and nonlocal stresses in particle migration, J. Non-Newton. Fluid 247 (2017) 229–238.

[34] S. Savage, M. Babaei, T. Dabros, Modeling gravitational collapse of rectangular granular piles in air and water, Mech. Res. Commun. 56 (2013) 1–10.

[35] M. M. Denn, J. F. Morris, Rheology of non-Brownian suspensions, Ann. Rev. Chem. Biomol. Eng. 5 (2014) 203–228.

[36] M. V. Papalexandris, A two-phase model for compressible granular flows based on the theory of irreversible processes, J. Fluid Mech. 517 (2004) 103–112.

[37] C. Varsakelis, M. V. Papalexandris, Low-Mach-number asymptotics for two-phase flows of granular materials, J. Fluid Mech. 669 (2011) 472–497.

[38] R. Hill, D. K. andd A.J.C. Ladd, The first effects of fluid inertia on flows in ordered and random arrays of spheres, J. Fluid Mech. 448 (2001) 213–241.

[39] S. Benyahia, M. Syamlal, T. O'Brien, Extension of Hill-Koch-Ladd drag correlation over all ranges of Reynolds number and solids volume fraction, Powder Tech. 162 (2005) 166–174.

[40] M. Massoudi, Constitutive relations for the interaction force in multi-component particulate flows, Int. J. Nonlinear Mech. 38 (2003) 313–336.

[41] S. L. Passman, Forces on the solid constituent in a multiphase flow, J. Rheol. 30 (1986) 167–192.

[42] K. Yeo, M. Maxey, Numerical simulations of concentrated suspensions of monodisperse particles in a poiseuille flow, J. Fluid Mech. 682 (2011) 491–518.

[43] J. Powers, D. Stewart, H. Krier, Analysis of steady compaction waves in porous materials, J. Appl. Mech. 59 (1989) 15–24.

[44] A. Chorin, A numerical method for solving incompressible viscous flow problems, J. Comput. Phys. 2 (1967) 12–26.

[45] R. Temam, Une méthode d'approximation des solutions des équations de Navier-Stokes, Bull. Soc. Math. France 98 (1968) 115–152.

[46] C. Rhie, W. Chow, Numerical study of the turbulent flow past an airfoil with trailing edge separation, AIAA J. 21 (1983) 1525–1532.

[47] C. Varsakelis, M. V. Papalexandris, A numerical method for two-phase flows of dense granular mixtures, J. Comput. Phys. 257 (2014) 737–756.

[48] C. Varsakelis, D. Monsorno, M. V. Papalexandris, Projection methods for two velocity-two pressure models for flows of heterogeneous mixtures, Comput. Math. Appl. 70 (2015) 1024–1045.

[49] S. Balay, et al., PETSc Web page, 2018. URL: `http://www.mcs.anl.gov/petsc`.

[50] E. Bueler, PETSc for Partial Differential Equations, SIAM, 2020.

[51] J. Morris, F. Boulay, Curvilinear flows of noncolloidal suspensions: The role of normal stresses, J. Rheol. 43 (1999) 1213–1237.

[52] A. Einstein, Eine neue bestimmung der moleküldimensionen, Ann. Phys. 19 (1906) 289–306. (in German).

[53] G. K. Batchelor, The effect of Brownian motion on the bulk stress in a suspension of spherical particles, J. Fluid Mech. 83 (1977) 97–117.

[54] R. Roscoe, The viscosity of suspensions of rigid spheres, Br. J. Appl. Phys. 2 (1952) 267–269.

[55] H. C. Brinkman, The viscosity of concentrated suspensions and solutions, J. Chem. Phys. 20 (1952) 571–581.

[56] I. Krieger, T. Dougherty, A mechanism for non-newtonian flow in suspensions of rigid spheres, Trans. Soc. Rheol. III (1959) 137–152.

[57] D. Quemada, Rheology of concentrated disperse systems and minimum energy dissipation principle - i. viscosity-concentration relationship, Rheol. Acta 16 (1977) 82–94.

[58] A. Dörr, A. Sadiki, A. Mehdizadeh, A discrete model for the apparent viscosity of polydisperse suspensions including maximum packing fraction, J. Rheol. 57 (2014) 743–765.

[59] F. Boyer, E. Guazzelli, O. Pouliquen, Unifying suspension and granular rheology, Phys. Rev. Lett. 107 (2011) 188301.

[60] F. Ferrini, D. Ercolani, B. D. Cindio, L. Nicodemo, L. Nicolais, S. Ranaudo, Shear viscosity of settling suspensions, Rheol. Acta 18 (1979) 289–296.

[61] G. K. Batchelor, J. T. Green, The determination of the bulk stress in a suspension of spherical particles to order c^2, J. Fluid Mech. 56(3) (1972) 401–427.

[62] G. MiDi, On dense granular flow, Eur. Phys. J. E 14 (2004) 341–365.

[63] P. Jop, Y. Forterre, O. Pouliquen, A constitutive law for dense granular flows, Nature 441 (2018) 73–727.

[64] L. L, K. R. R., Axisymmetric granular collapse: a transient 3d flow test of viscoplasticity, Phys. Rev. Lett. 102(10):108305 (2009).

[65] J. Stickel, R. Powell, Fluid mechanics and rheology of dense suspensions, Annu. Rev. Fluid Mech. 37 (2005) 129–149.

[66] J. F. Brady, A. S. Khair, M. Swaroop, On the bulk viscosity of suspensions, J. Fluid Mech. 554 (2006) 109–123.

[67] M. Holmes, N. Parker, M. Povey, Temperature dependence of bulk viscosity in water using acoustic spectroscopy, J. Phys. Conf. Ser. 269 (2011) 012011.

[68] F. Radjai, V. Topin, F. Perales, Y. Monerie, Tumbling sandpiles in a fluid, in: AIP Conference Proceedings, volume 1542, 2013, p. 662.

[69] M. Shademani, B. Blais, A. Shakibaeinia, Cfd-dem modeling of dense sub-aerial and submerged granular collapses, Water 13 (2021) 2969.